

NATIONAL INSTITUTE FOR FUSION SCIENCE

Detection of Kinetic Geodesic Acoustic Mode (KGAM) near the  
Center Region of JIPPT-IIU Tokamak Plasmas

Y. Hamada, T. Watari, A. Nishizawa, O. Yamagishi, K. Narihara, K. Ida,  
Y. Kawasumi, T. Ido, M. Kojima, K. Toi and JIPPT-IIU Group

(Received - July 20, 2010 )

NIFS- 961

Aug. 3, 2010

RESEARCH REPORT  
NIFS Series

**Detection of kinetic geodesic acoustic mode (KGAM)  
near the center region of JIPPT-IIU Tokamak Plasmas**

Y. Hamada\*, T. Watari, A. Nishizawa, O. Yamagishi, K. Narihara, K. Ida, Y. Kawasumi,  
T. Ido, M. Kojima, K. Toi and JIPPT-IIU Group  
*National Institute for Fusion Science, Toki, 509-5292, Japan*

(Received )

The broad and intense spectrum of the geodesic acoustic mode (GAM) oscillations near the magnetic axis of the tokamak plasmas with  $T_e/T_i \gg 1$  becomes narrow and weak during neutral beam heating. It then becomes wide and weak during third harmonics ICRF heating. The wide spectra of GAMs are generally consistent with recent kinetic GAM (KGAM) theories.

Keywords: tokamak, geodesic acoustic mode, GAM, KGAM, drift wave, HIBP, JIPPT-IIU  
DOI: PACS numbers: 52.35.Ra

The “drift wave-zonal flow paradigm“, in which zero-frequency zonal flows generated by drift-wave turbulence provide the dominant mechanism of the nonlinear saturation of the drift-wave turbulence, is one of the most important topics related to the physics of the confined plasmas [1-10]. It was first stated by Hasegawa *et al.*, evaluating the similarity of equations of drift waves in the confined plasma and Rossby waves in an atmospheric pressure system [1, 2]. For an extensive review of zonal flows see ref. [10].

Since this paradigm was first verified using large-scale computer simulations of the tokamak plasmas [7] in which electron components are treated as adiabatic, the modification of this paradigm may be necessary for plasmas where the effect of trapped electrons is important. In this sense, the applicability of this paradigm to the plasmas dominated by trapped electron mode instability (TEM) [11], has been intensively discussed [12-16]. Experimentally, using a heavy ion beam probe (HIBP) both we and the TEXT group [17-23], detected intense potential oscillations of zonal flow of another type, high-frequency zonal flows (geodesic acoustic mode, GAM [8, 24]) in the core region of OH tokamak plasmas, where  $T_e/T_i \gg 1$ . However, the first experimental paper on GAMs by the TEXT group suggested the observed GAMs ( $m=0$ ) to be an artefact of the HIBP, instead of natural modes generated by mode coupling of drift tearing mode ( $m \approx 12$ ) [17]. We found that in the core of low-density OH plasmas, the Fourier spectra of the signals of multi-channel ECE, soft-xray signals and reflectometer have no peaks corresponding to GAM oscillations with the amplitude of GAMs about a few 100 Vp-p. This fact can be understood by the fact that GAMs are pure poloidal rotation of  $m=0$  and has almost no effect on the temperature and the density in the center of the plasma. In addition, we verified it as real potential oscillations or the acceleration of the HIBP beam by time derivative of magnetic vector potential [18]. Still later we proved that the observed strong potential oscillation in the low-density OH plasmas are real potential oscillations of  $m=0$ , since the acceleration of the beam by vector potential injected perpendicular to the magnetic field, is negligible in low-beta plasma [19].

Recently computer simulations in which both ions and electrons are treated by gyrokinetic equations have shown that the high-frequency zonal flow (GAM) can be as effective as the low-frequency zonal flows in the determination of the turbulence level of drift-wave turbulence [16]. Although GAMs are ineffective in the regulation of the drift-wave turbulence through shearing effect, because the drift-wave

frequency is comparable to the GAM frequency, GAM may be important as the reservoir of the energy flow from the drift-wave turbulence via three-wave coupling [16]. Then GAMs become damped through linear Landau damping. In this paper, the frequency of GAM is very wide, meaning the energy reservoir of turbulence energy of drift waves. Recently we have verified experimentally that the GAM is excited by drift-wave turbulence through three-wave coupling [23].

Experimentally up to now GAM zonal flows have been characterized mostly by a narrow and weak (a few times larger than the background turbulence) spectrum in the outer layer of the tokamak plasmas, where the safety factor ( $q$ ) is high and the damping rate is low [25-28]. In this paper we show that in the center region of low-density OH plasmas with  $T_e/T_i \gg 1$ , a very wide and intense spectrum which extends from 20 kHz to 50 kHz, of potential oscillations of  $m=0$  is observed and this wide spectrum can be explained by the kinetic GAM theories [29-35]. In addition, there occurs a drastic change of the GAM spectrum, to weak and narrow spectrum in NBI heated plasmas and to weak and wide spectrum in ICRF heated plasmas. The wide spectrum of kinetic GAM oscillations may mean the large energy flow from the drift-wave turbulence through nonlinear interactions between GAM and turbulence. It also may provide the dominant nonlinear saturation mechanism of the drift-wave instability and the regulation of the turbulence, which is one of the most important topics in the study of the plasma confinement.

To study these phenomena a heavy ion beam probe (HIBP) may be an ideal diagnostic [17-22]. Using HIBP zonal flows can be determined through fast, local and multi-point measurement of plasma potential ( $\Phi$ ) since zonal flows are  $E/B (= -\nabla\Phi \times B/B^2)$  drift motions [1,2].

The experiment was carried out in JIPP T-IIU tokamak plasmas with nearly circular cross-section and with major and minor radii of 93 cm and 23 cm, respectively [36]. We analyzed the shot of NBI heating and ICRF  $3-\omega_{ci}$  heating and current drive (H/CD) with a phased 12-strap antenna on the smaller major radius side [37].

The HIBP for the JIPP T-IIU tokamak injects a 50-500 keV thallium ( $Tl^+$ ) beam [18]. The intensity of the secondary beam ( $Tl^{++}$ ) ionized at a sample volume (SV) is proportional to local density and the change of the energy corresponds to the local plasma potential at the SV. The position, size and direction of alignment of 6 SVs used in this experiment are shown in Fig. 1(a). SVs are specified by three parameters, i.e., primary beam energy ( $j=A, B, \text{ and } C$ , for 450, 300, and 250 keV, respectively, under a toroidal magnetic field of 3T), poloidal injection angle ( $k=1-6$ ), and input slit number of an energy analyzer ( $l=1-6$ ). A set of partial lines, designated by 2 labels (energy and injection angle) like A2, is called "a step" in this paper. Figure 1(b) shows an expanded view of what the SVs look like at step A4. The SVs are cylinders of about 2-4 mm in diameter, cut at a slant angle with a side appearance of a parallelogram. The length of the longer diagonal of the parallelogram, ( $l_s$ ) is about 5 to 15 mm, depending on the energy and injection angle. It is nearly parallel to the beam trajectory and strongly reduces the signal level of the density fluctuations whose wavelength along the trajectory is comparable to  $l_s$  through integration on  $l_s$  [38]. This reduction deforms the wavelength spectrum of the turbulence and also helps to reduce the spatial aliasing effect. The frequency bandwidth of the detector circuit at 3db gain decrease is 300 kHz.

Plasma current was 130 kA with a safety factor  $q$ -value around 6 and toroidal field of 3T. The center electron temperature of the deuterium plasma rises to 1.0 keV (Fig. 1(c), 1(e)) and ion temperature to about 200 eV (Fig. 1(e)) in the core by Ohmic heating when the average plasma density is low to about  $0.7 \times 10^{13}/\text{cm}^3$ . At 170 ms, about a quarter of a MW hydrogen (30 kV) NBI power is injected for a duration of about 100 ms. Then ICRF  $3-\omega_{ci}$  heating/current-drive (H/CD) is conducted. The total plasma energy measured by plasma diamagnetism increases from 2 kJ to 4-5 kJ and the average plasma density increases to about  $2 \times 10^{13}/\text{cm}^3$  due both to the strong plasma-surface (antenna) interaction during the

heating period and to the gas puffing used to suppress MHD oscillations. The electron temperature rises during NBI heating to about 1.2 keV and ion temperature measured by fast neutral energy analyzer (FNA) rises to about 0.6-0.7 keV (Fig. 2(e)). However, FNA temperature tends to give lower ion temperature at higher plasma density and the ion temperature measured by charge-exchange spectroscopy is about 800 eV,

Figure 2(a) shows the temporal change of the Fourier spectrum of the potential with 1 ms duration at SV3 of A3. Before the start of NBI heating, a very wide and intense spectrum which extends from 20 kHz to 60 kHz is observed [18, 21-23]. This potential spectrum and that of Fig. 2(b) are far above the level of the potential of the drift-wave turbulence. This spectrum is in clear contrast to the density fluctuation spectrum shown in Fig. 2(c), where the drift-wave turbulence is dominant and extends to about 500 kHz.

This wide spectrum of potential oscillations can be ascribed to kinetic GAM oscillations because of following reasons. 1) The phase difference of potentials at SV4 and SV5 is small as shown in Fig. 2(d) in sharp contrast to the large phase difference of the density oscillations shown in Fig. 2(e). 2) Density spectrum has almost no influence of the intense potential oscillations as shown in Fig. 2(c) except the high frequency end of the potential oscillations, while  $m=1$  or 2 MHD oscillations has large reactions on both density and potential signals. In case of Fig. 2(f)-(h), SVs are at around A4, and the reaction on the density spectrum is very small as shown in Fig. 2(g). Since the aspect-ratio at A4 is almost 25, the density fluctuations caused by pure poloidal rotations are very small in agreement with the observation and in sharp contrast to other MHD oscillations. 3) These potential oscillations are very robust and in almost all discharges, we can observe this wide spectrum, while usual MHD oscillations can be easily stabilized by the change of plasma current or the change of waveforms of gas puffing. 4) Usually MHD oscillations in the hot-core of the plasma can be easily detected by the ECE or soft-X ray array signals. The typical example is sawtooth oscillations. However, we can't find the effect of the wide spectrum observed by HIBP, in ECE, soft-X ray signals as shown in Figs. 2(i)-2(m). It may be due to the fact that GAM induces pure poloidal rotations and the potential oscillations with observed wide spectrum belong to GAM. 5) We routinely suppress usual MHD low-frequency oscillations, Mirnov oscillations for example, using control knobs such as gas puffing, plasma current, or shift of the plasma center in the vacuum vessel, since they have severe deteriorating effect on the plasma temperature or plasma confinement. HIBP signals are also severely affected since Mirnov oscillations induce large density and potential oscillations. It is not hard to have stable tokamak OH discharge shown in Fig. 1(c) and (d) free from low-frequency MHD oscillations. 6) GAM theory requires phase relations between poloidal rotation  $V_*$  and  $\tilde{n}_e$  [24] and it leads in high-aspect-ratio limit to phase relation of  $d\tilde{\Phi}/dr \propto i\tilde{n}_e/\bar{n}_e$  in our case where  $d\tilde{\Phi}/dr$  is the radial derivative of plasma potential. Figure 2(h) shows the phase of  $\langle(\phi(3)-\phi(4))(\tilde{n}_e(3)+\tilde{n}_e(4))\rangle$ . It shows clear phase relations in right sense between them. The phase of  $i=(0,1)$  is  $\pi/2$  and a little smaller than the observed rise of the phase at GAM band. It is however, due to the fact that our measurement is not 2 dimensional and HIBP signals are composed of GAMs and drift-wave turbulence. 7) It is interesting to note that the ECE spectra near the A4 shows clear rise of spectra near  $2f_{\text{GAM}}$  while there is no reaction at  $f_{\text{GAM}}$ . This may mean that the GAM induces good effect on the plasma confinement on each polarity of the rotation, leading to the rise of ECE at double frequency. We want to discuss this phenomenon in a separate paper because it may be a very complex phenomenon.

At A4-A5, the alignment of SVs is approximately along the poloidal magnetic surface and the phase difference of the density signals is large and we can measure the frequency dependence of the poloidal wavelength (dispersion of the turbulence) in Fig. 2(e).

In a few milliseconds after the start of NBI heating the spectrum of GAM oscillations damps and a weak and narrow peak at about 30 kHz appears throughout NBI, and after the start of ICRF H/CD it becomes wider again, as is also shown in the red (NBI phase) and blue (ICRF phase) curves of Fig. 2(b).

The positive phase difference of the density signals at frequencies larger than 50 kHz, in Fig. 2(e) shows that the dominant density turbulence propagates to the electron diamagnetic drift direction, and we may be able to ascribe this to trapped electron mode (TEM) turbulence [11]. The red curve of Fig. 2(d) and 2(e) show that the phase is noisy but negative around 10-20 kHz meaning there is a component propagating to ion diamagnetic drift direction (ion temperature gradient mode, ITG) in the low-frequency region, leading to the coexistence of ITG and TEM [22].

The potential oscillations are composed of both GAM and drift-wave turbulence. Accordingly the measured phase difference (Fig. 2(d)) may be  $\delta\Phi_d I_d/I_{\text{GAM}}$ , in case of  $I_d/I_{\text{GAM}} \ll 1$  due to the phase difference ( $\delta\Phi_d$ ) in the drift-wave turbulence.  $I_d/I_{\text{GAM}}$  is the ratio of the intensity of the drift-wave intensity to the GAM intensity. We can estimate this ratio to be about 0.03 when we draw the potential spectrum in logarithmic scale in Fig. 2(b), and estimate the level of drift-wave turbulence at the region of 20 kHz to 60 kHz where GAMs are dominant. Also at A4 It may be due to the radial wavenumber of the GAM since the alignment of the SVs at A4 and A5 may have small radial component. We have to be careful in the interpretation of observed small positive phase difference since it is influenced by 4 factors, the radial and poloidal wavenumbers of GAM and drift-wave turbulence.

At A3 or A2 the direction of the alignment of the SVs is almost radial and the measured phase difference becomes large. In this region the level of the drift wave and the ratio of  $I_d/I_{\text{GAM}}$  becomes larger and the phase is easily affected by the characteristics of the drift-wave turbulence.

In order to interpret the wide spectrum of GAM oscillations, we utilize the dispersion relation derived by Zonca et al. [33, 39]. It was first derived in 1996 for that of beta-induced Alfvén eigenmode (BAE). Since Garbet noted the degeneracy of BAE and GAM [40], this equation can be useful for the analysis of kinetic GAM. Gao et al. derived similar formula in 2008. Watari has derived a kinetic GAM equation even taking into consideration the effect of trapped particles [35]. We may analyze the data using Watari's formula in a separate paper. In addition, in this paper, the center area has very high aspect-ratio and the effect of the trapped particles may not be critical. Accordingly we use Zonca's formulas for kinetic GAM, His equation is as follows [33],

$$\Lambda_0(\Omega) - (k_r \rho_i)^2 \Lambda_1(\Omega) = 0 \quad (1)$$

where  $\Lambda_1 = 3/4 + q^2 S_0 / \Omega$ ,  $\Lambda_0 = 1 + q^2 (F - N^2 / D) / \Omega$ ,

$$S_0(\Omega) = \frac{q^2}{2\Omega^2} \left[ L - 2L_2 - \frac{2N}{D} (H - 2H_2) + \frac{N^2}{D^2} (F - 2F_2) \right] + T - \frac{2N}{D} V + \frac{N^2}{D^2} Z + \frac{q^2}{\Omega^2 D_2} \left[ F_2 - F - \frac{N}{D} (N_2 - N) \right]^2,$$

$$D = (1 + T_i / T_e) \Omega^{-1} + Z(\Omega), \quad N(\Omega) = \Omega + (\Omega^2 + 1/2)Z(\Omega), \quad F = F(\Omega) = \Omega(\Omega^2 + 3/2\Omega) + (\Omega^4 + \Omega^2 + 1/2)Z(\Omega),$$

$$V = \Omega + (\Omega^2 + 1)Z(\Omega), \quad L = \Omega^7 + (5/2)\Omega^5 + (19/4)\Omega^3 + (63/8)\Omega + (\Omega^8 + 2\Omega^6 + 3\Omega^4 + 3\Omega^2 + 3/2)Z(\Omega),$$

$$H(\Omega) = \Omega^5 + 2\Omega^3 + 3\Omega + (\Omega^6 + (3/2)\Omega^4 + (3/2)\Omega^2 + 3/4)Z(\Omega),$$

$$T(\Omega) = \Omega^3 + (5/2)\Omega + (\Omega^4 + 2\Omega^2 + 3/2)Z(\Omega),$$

$$N_{1/2} = N(\Omega/2), \quad F_{1/2} = F(\Omega/2), \quad \Omega = \omega q R / v_{ti}, \quad Z(\Omega) \equiv \pi^{-0.5} \int_{-\infty}^{\infty} \frac{e^{-y^2}}{y - \Omega} dy.$$

$\rho_i$  is the ion gyroradius and  $\Omega = \omega q R / v_{ti}$ ,  $v_{ti}^2 = T_i / M$ .

Figures 3(a)-3(g) show the real and imaginary  $(k_r \rho_i)^2$  as a function of normalized frequency,  $\Omega' (= \Omega (T_i / T_e)^{0.5} / q)$  using the dispersion relation  $(\Lambda_0 - \Lambda_1(k_r \rho_i)^2 = 0)$  for six cases of various ratio of  $T_i / T_e$  and  $q$ . We changed  $\Omega$  to  $\Omega'$  since  $\Omega (= \omega q R / v_{ti})$  is a function of  $q$  and  $T_i$  while the actual GAM frequency  $\omega_{\text{GAM}}$  may scale as  $\omega_{\text{GAM}} \propto R / v_s$ ,  $v_s = ((T_e + T_i) / M)^{0.5}$  as is shown by Lebedev et al. [29]. The kinetic GAM frequency ( $\Omega_k$ ), defined by  $\Lambda_0 = 0$ , is an important value and is given by  $\Omega_k^2 = q^2(7/4 + T_e / T_i) + (1/2) T_e / T_i$  for high  $q$  limit.

In the case of  $T_i / T_e = 0.1$ ,  $q = 1.5$  (Fig. 3(d)), the kinetic GAM theory predicts Landau damping will be rather small and there will exist a wide frequency range of GAM oscillations nearly from  $\Omega_k$  to lower frequency ( $\approx \Omega_k / 2$ ) with small Landau damping and propagation mode  $(k_r \rho_i)^2 > 0$ . We assumed about  $q = 1.5$  because the low-density plasma with 130 kA has no sawtoothing phenomena while 200 kA discharge has sawtooth oscillations with about 12 cm-diameter inversion radius. In addition, a clear and wide GAM spectrum is also observed in 200 kA discharges.

As  $T_i$  increases to  $T_i / T_e = 0.2$  (Fig. 3(a), OH phase as shown in Fig. 1(e)), the damping rate increases near the middle of the red horizontal line on the  $(k_r \rho_i)^2 = 0$ , indicating the propagation range. The double peaked spectrum in Fig. 2(b) may be explained in this way if the driving term by the density turbulence is homogeneous. The waveform of  $k_r \rho_i$  of Fig. 3(a) may be similar to the observed phase of Fig. 3(a), since the alignment of SVs near A4 is not purely poloidal and may have radial component. However, as was mentioned before,  $I_d / I_{\text{GAM}}$  causes serious distortion in the GAM phase measurement.

As  $T_i$  increases to  $T_i / T_e = 0.6$  (Fig. 3(b), NBI heated phase), the damping rate increases about 5 times compared with that of Fig. 3(a). We may assume that the single potential spectrum peak in the NBI phase (red curve of Fig. 2(b)) may correspond to the lower end of the red horizontal line. Another possibility is the observed weak GAM may be due to the energetic-particle-induced GAM (EGAM) [41, 42]. The weak and wide spectrum during ICRF heating may be explained by Fig. 3(c) of  $T_i / T_e = 1$ . The spectrum of propagation in Fig. 3(c) may be wider compared to Fig. 3(a), while the observed spectra are similar. This may be due to the strong Landau damping.

As is shown by the red horizontal lines in Fig. 3(d-e), the range of propagation,  $(k_r \rho_i)^2 > 0$  and smaller damping, becomes narrower when  $q$  value becomes larger in the case of  $T_i / T_e = 0.1$ . This result is universal for higher ratio of  $T_i$  to  $T_e$ . This may explain the fact that the experimentally observed GAM oscillations up to now has narrow spectrum with the exception of oscillations we have observed in the center region of tokamak plasma.

In summary, the wide GAM spectrum in about  $r/a_p = 0.2$  core region of the low-density OH plasmas are in agreement with the prediction of linear kinetic GAM theory by Zonca *et al.* [33]. The narrow spectrum in the outer area with high  $q$  number can be also explained by the theory. Narrow and weak spectrum during NBI may be due to EGAM.

## Acknowledgement

This work is partially supported by Ministry of Science and Education of Japan under contracts 21246140 and JSPS Japan-China core-university program.

\* Also at Sokendai, Graduate University for Advanced study, Hayama, 240-0163, Japan

- 
- [1] Hasegawa A. *et al.*, Phys. Fluids **22**, 2122 (1979).
- [2] A. Hasegawa, and M. Wakatani, Phys. Rev. Lett. **59**, 1581 (1987).
- [3] P.H. Diamond and Y.-B Kim, Phys. Fluids **B3** 1626 (1991).
- [4] G.W. Hammett, Plasma Phys. Control. Fusion **35** **973** (1993).
- [5] V.B. Lebedev *et al.*, Phys. Plasma **2**, 4420 (1995).
- [6] P. H. Diamond *et al.*, in *Proceedings of the 17th IAEA Fusion Energy Conference, Yokohama, 1998* (International Atomic Energy Agency, Vienna, Austria, 1999), Vol. **4**, pp. 1421–1428.
- [7] Z. Lin *et al.*, Science **281**, 1835 (1998).
- [8] K. Hallatschek and D. Biskamp, Phys. Rev. Lett. **86**, 1223 (2001).
- [9] B. Scot, Phys. Lett. A **320**, 53 (2003).
- [10] P.H. Diamond *et al.*, Plasma Phys. Control. Fusion **47**, R35 (2005).
- [11] G. Rewoldt and W.M. Tang, Phys. Fluids **B 2**, 318 (1990).
- [12] T. Dannert and F. Jenko, Phys. Plasmas **12**, 072309 (2005)
- [13] J. Lang *et al.*, Phys. Plasmas **15**, 055907 (2008).
- [14] A.G. Peeters *et al.*, Phys. Plasmas **12**, 022505 (2005).
- [15] D.R. Emst *et al.*, Phys. Plasmas **11**, 2637 (2004).
- [16] R.E. Waltz and C. Holland, Phys. Plasmas **15**, 122503 (2008).
- [17] H.Y. Tsui *et al.*, Phys. Fluids **B 5**, 1274 (1993).
- [18] Y. Hamada *et al.*, Fusion Engineering and Design **34-35**, 663 (1997).
- [19] Y. Hamada *et al.*, Nucl. Fusion **36** 518 (1997).
- [20] P.M. Schoch *et al.*, Rev. Sci. Instrum. **74**, 1846 (2003).
- [21] Y. Hamada *et al.*, Nucl. Fusion **45**, 81 (2005).
- [22] Y. Hamada *et al.*, Phys. Rev. Lett. **99** 065005 (2007).
- [23] Y. Hamada *et al.*, Nucl. Fusion **50**, 81 (2010).
- [24] N. Winsor *et al.*, Phys. Fluids **11**, 2448 (1968).
- [25] G.R. McKee *et al.*, Plasma Phys. Control. Fusion **45**, A477 (2003).
- [26] T. Ido *et al.*, Nucl. Fusion **46**, 512 (2006).
- [27] G. D. Conway *et al.*, PPCF **47**, 1165 (2005).
- [28] D.K. Gupta *et al.*, Phys. Rev. Lett. **97**, 125002 (2006).
- [29] V.B. Lebedev Phys. Plasmas **3**, 3023 (1996).
- [30] T. Watari *et al.*, , **12** 062304 (2005).
- [31] H. Sugama and T.-H. Watanabe, **13**, 062504 (2006).
- [32] T. Watari *et al.*, Phys. Plasmas **13**, 062504 (2006).
- [33] F. Zonca and L. Chen, Euro. Phys. Lett. **83**, 35001 (2008).
- [34] Z. Gao *et al.*, Phys. Plasmas **15**, 072511 (2008).
- [35] T. Watari *et al.*, Phys. Plasmas **14**, 112512 (2007).
- [36] K. Toi *et al.*, Plasma Physics and Controlled Nuclear Fusion Research, 1992 (Proc. 14<sup>th</sup> Int. Conf. Wurzburg, 1992), Vol. 1, IAEA, Vienna ) 519 (1993).
- [37] T. Seki *et al.*, Nuclear Fusion **32**, 2189 (1992).
- [38] Y. Hamada *et al.*, Nucl. Fusion **37**, 999 (1997).
- [39] F. Zonca *et al.*, Plasma Phys. Control. Fusion **38**, (1996).2011.
- [40] X. Garbet *et al.*, in Theory of Fusion Plasmas, edited by J.W. Connor, *et al.*, Vol. **CP871** (AIP, NY) p.342 (2006).
- [41] C.J. Boswell *et al.*, Phys. Lett A **358**, 154 (2006).
- [42] R. Nazikian *et al.*, Phys. Rev. Lett. **101**, 185005 (2008).

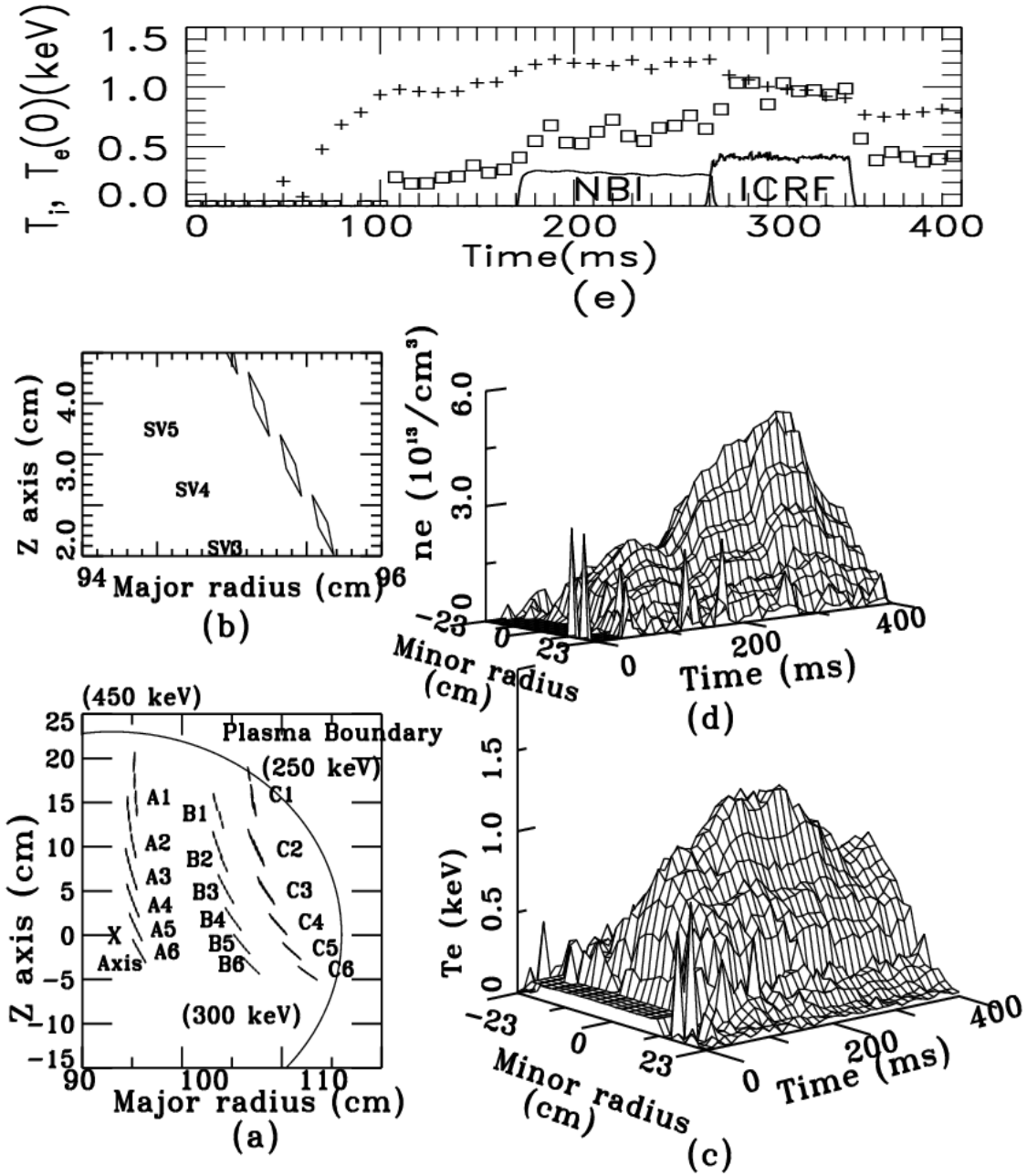


FIG. 1. (a) Location and direction of alignment of 6 SVs of the HIBP at 18 steps. The label A stands for the beam energy of 450 eV, label B for 300 keV and label C for 250 keV. (b) Shape and positions for SVs at step A4. (c)–(e) show the temporal changes of radial profiles of electron temperature (c) and density (d) measured by the Thomson scattering apparatus and (e) shows the ion temperature measured by square mark using fast neutral energy analyzer. + shows the electron temperature at the magnetic axis,  $r=0$ .

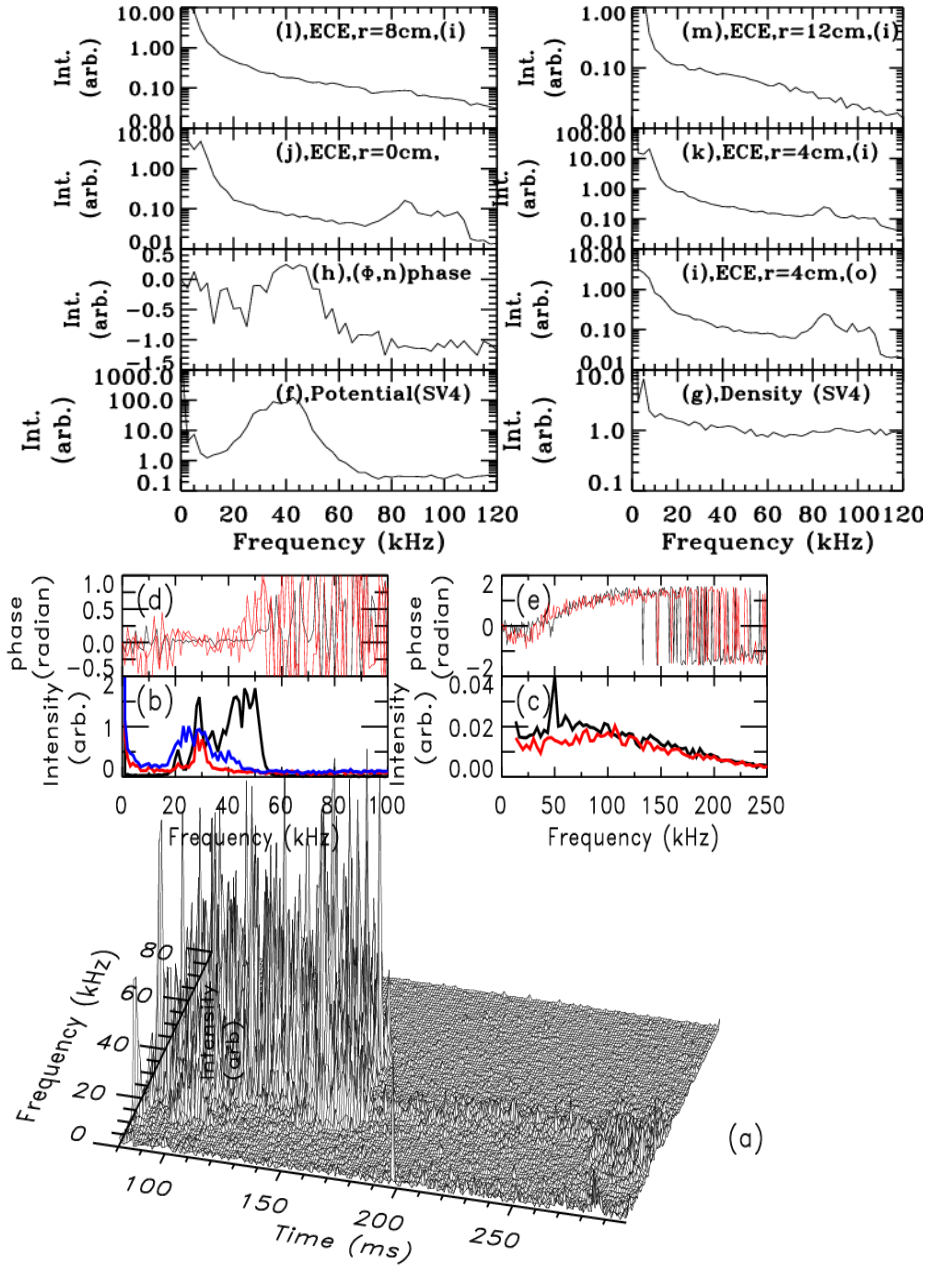


Figure 2(a) shows the temporal change of the potential spectra at every one millisecond interval. (b) and (c) show the potential Fourier spectrum (b) and that of density (c) in OH phase (black curve) and NBI phase (red). In Fig. 2(b) the red and blue curve (ICRF phase) is multiplied by the factor of 10. (d) and (e) shows the phase difference of the potential signals at SV3 and SV4 (d) and the density signals respectively. The black line is for 140-170 ms (OH), red curve for 180-210 ms (NBI) and blue one for 270-300 ms. The blue curves in (c)-(f) are omitted because those are noisy due to the severe attenuation of the HIBP beam in the high density plasmas. Figures 2(f)-2(m) show the Fourier spectra of HIBP and ECE signals of 200 kA low-density OH plasmas. (f) and (g) are for spectra of HIBP potential and density on SV4 around step A4. 2(h) shows the phase of  $\langle (\phi(5) - \phi(4)) (\tilde{n}_e(5) + \tilde{n}_e(4)) \rangle$ , the phase between radial gradient of potential, corresponding to the poloidal flow and density turbulence. (i) –(m) are for ECE signals at  $r=4$  cm (larger major radius)(i),  $r=0$  cm (magnetic axis, (j), and 4 cm,(k), 8 cm, (l) and 12 cm, ( $r=12$  cm) respectively. Figures 2(k)-2(m) are for smaller major radius side and are denoted by signs of (i).

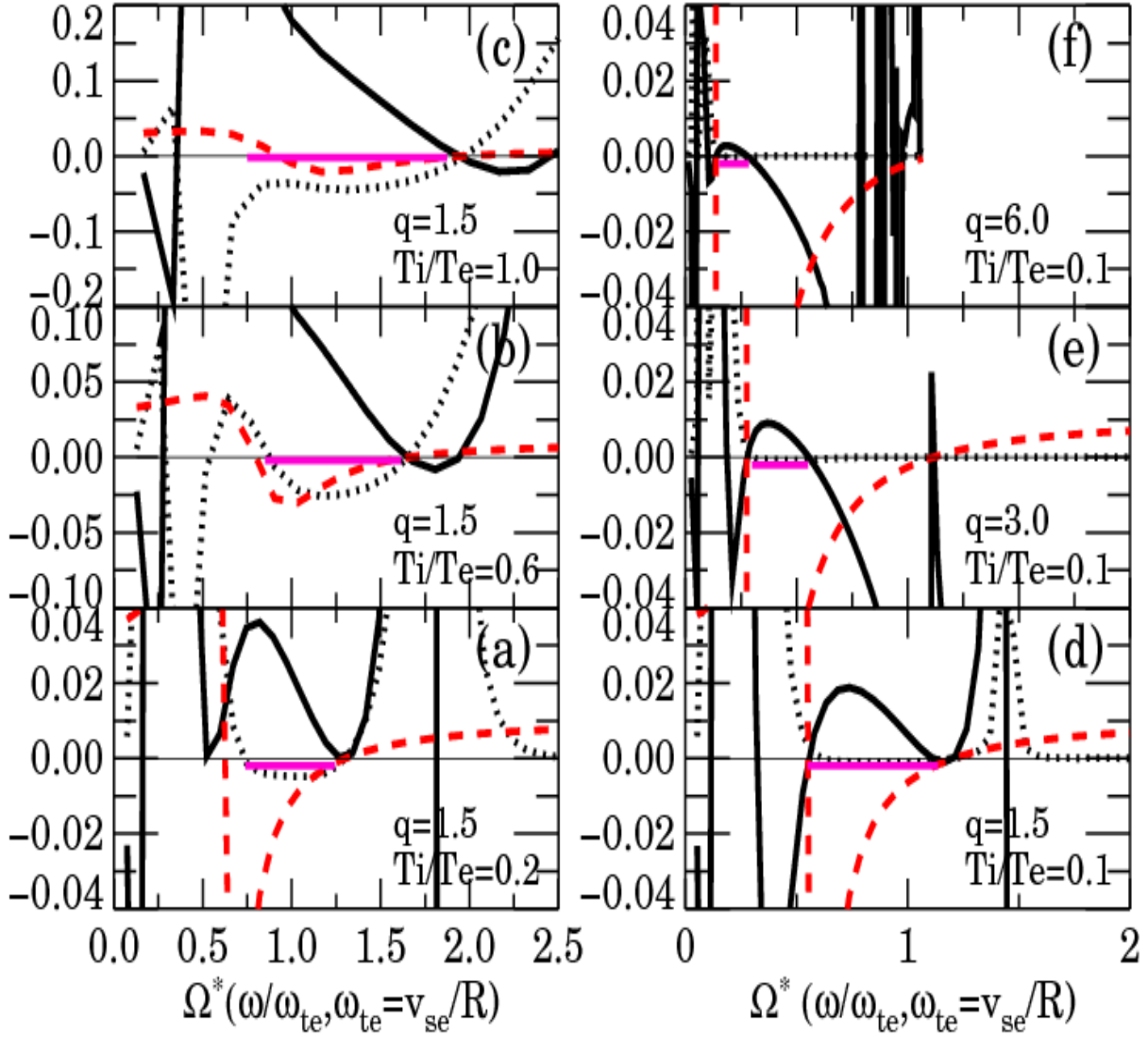


Figure 3. Frequency dependence of  $(k_r \rho_i)^2 = \Lambda_0(\Omega') / \Lambda_1(\Omega')$ ,  $\Omega' = \omega R / v_{te}$ . The solid curve is real part and the dashed one is for an imaginary part. The red dashed curve is real  $\Lambda_0(\Omega')/100.0$ . The red horizontal solid line indicates the region of  $(k_r \rho_i)^2 > 0$ , region of propagation.